Materials selection of steam-phase change material (PCM) heat exchanger for thermal energy storage systems in direct steam generation facilities

F. Javier Ruiz-Cabañas[1,*], Aleix Jové[1], Cristina Prieto[1], Virginia Madina[2], A. Inés Fernández[3], Luisa F. Cabeza[4]

[1]Abengoa Research, C/ Energía Solar nº 1, Palmas Altas, 41014, Sevilla, Spain

[2]Materials for Energy and Environment Unit. Tecnalia Research and Innovation, Mikeletegi Pasealekua, 2, 20009 San Sebastián, Spain

[3]Department of Materials Science & Physical Chemistry, Universitat de Barcelona, Martí i Franqués 1-11, 08028 Barcelona, Spain

[4]GREA Innovació Concurrent, Universitat de Lleida, Edifici CREA, Pere de Cabrera s/n, Lleida, Spain

* Corresponding author:

F. Javier Ruiz-Cabañas

Abengoa Research, C/ Energía Solar nº 1, Palmas Altas, 41014-Sevilla

Phone: 0034954996570

Cell: 0034618125761

Email: fjavier.ruiz@abengoa.com

Abstract

Phase change materials (PCM) is one of the most interesting solutions to be used in thermal energy storage (TES) systems for direct steam generation (DSG) thermosolar facilities. Properties such as high energy density and energy storing/delivery at constant temperature bring PCM based systems in excellent candidates for DSG facility storage units. Accordingly, LiOH-KOH peritectic mixture, with a melting point of 315 ºC and an enthalpy change of 535 kJ/kg, has been reported as attractive solution for the saturated storage module in DSG plants. A steam-PCM heat exchanger is the critical component to carry out the thermal transference between both substances. Although materials selection to be applied for steam applications is well known, lack of knowledge is detected in the field of high temperature hydroxides corrosion. Therefore, three metallic materials, A516 Gr70 carbon steel, A316L stainless steel and Inconel 625 Ni-base alloy, have been evaluated to determine their corrosion performance after hydroxides exposure. While A516 Gr70 was discarded for this application due to high corrosion rates, A316L and Inconel 625 displayed good corrosion resistance after 2640 hours. Finally, A316L stainless steel was selected as potential candidate for the construction of the steam-PCM heat exchanger considering cost and thermal efficiency optimization.

Keywords: Corrosion, solar energy, direct steam generation (DSG), thermal energy storage (TES), phase change material (PCM), hydroxides

1. Introduction

Thermal energy storage (TES) in thermosolar industry is one of the main distinguishing factors to make the technology feasible [1-3]. Decoupling the peak energy demand time frame from the hours with maximum solar irradiation is crucial to integrate this technology in an efficient manner to the market [4-6]. One of the main emerging TES technologies within the thermosolar industry is the latent heat storage using phase change materials because it offers interesting characteristics in terms of energy density and heat exchange. The first advantage of those systems is the large energy density they have in comparison with systems working in the sensible region. The second interesting and peculiar characteristic is that PCM based systems deliver energy at constant temperature. This is an important difference regarding sensible heat solutions which store and deliver energy while changing its temperature [7-9].

PCM solutions have been usually related with direct steam generation (DSG) technology because their property of storing and delivering energy at a given temperature. Since steam exchanges heat at constant temperature when evaporates and condensates, the heat exchanged between a PCM and the steam requires less temperature differences between the storage media and the steam minimizing the exergy destruction [10-12]. Another important parameter of PCM systems is the melting point of the substance which is directly related with the steam discharge pressure in DSG technology. For a given melting point and temperature difference between the PCM and the steam, the evaporation pressure would be also fixed. Accordingly, maximum commercial Rankine power cycle efficiencies have been reported around 120 bar being the associated discharge temperature close to 324 ºC and maximum temperature of superheated steam around 550 ºC [13,14].

Important efforts have been done trying to integrate the PCM technology within the DSG solar power generation (Fig. 1a). One of the most studied solutions has been to split the TES system in three different units depending on the water/steam conditions: pre-heater, evaporator and superheater [15]. Feldhoff et al. [16] studied different alternatives to solve the TES system combining sensible and PCM subsystems. While latent heat related to the steam evaporation is always given by a PCM system, the sensible heat associated to water preheating and steam superheating could be solved with different solutions: (i) Concrete blocks, (ii) PCM and (iii) Molten salts storage tanks (Fig. 1b). In this way, an interesting DSG plant storage system would integrate a PCM system for preheating and evaporating and a configuration of two molten salt tanks for superheating the steam (Fig. 1b).

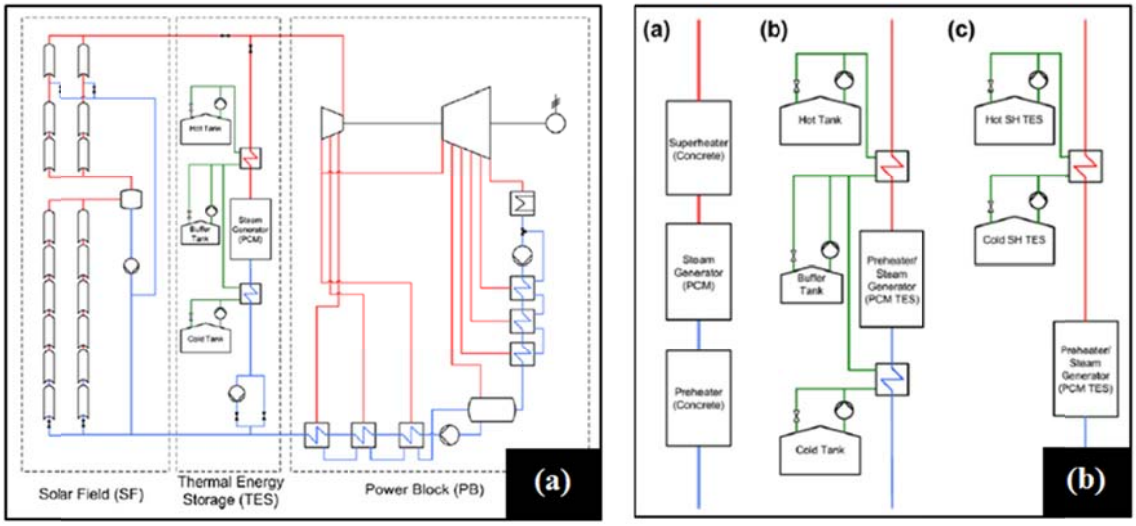

Fig. 1. DSG plant configuration: (a) Overall layout of DSG plant with TES system integrated, (b) TES configurations alternatives for DSG technology [16]

An improvement of the systems described before with an innovative configuration based on molten salt tanks and a PCM system was proposed to maximize the superheated steam discharge temperature using only two molten salt tanks and one PCM system [17]. This configuration would allow preheating and superheating the steam with sensible heat supplied by the molten salt tanks and to evaporate with the PCM system avoiding the use of the intermediate tank proposed on [15]. The next development found in the state of the art related with this concept is an innovative and high efficient design of a PCM system [18], which could be integrated in the plant configuration proposed by Birnbaum et al. [15]. The PCM solution consisted in a shell and tube heat exchanger between the process water/steam and the PCM. While the shell side contains a PCM material which has an adequate melting point in order to produce steam at the desired pressure, the tube side would contain the process water/steam.

In relation with the PCM material itself, the main efforts in the development of new efficient TES systems for DSG technologies based on PCM have been recently focused on finding high solutions with melting temperatures close to those 324 ºC trying to match power cycles at 120 bar. One of the most studied materials for those systems has been $NaNO_3$ with a melting point of 312 ºC and an enthalpy change of 170 kJ/kg. On the other hand, some authors have been focused on different PCM solutions such as NaOH (77.2%wt) – NaCl (16.2%wt) – Na_2CO_3 (6.6%wt) mixture with a melting point of 318 ºC and an enthalpy change of 290 kJ/kg which it seemed in advance an interesting alternative [19]. In parallel but also in this sense, Abengoa published a patent which proposes a composite based in an inorganic mixture of LiOH (46%wt) and KOH (54%wt) infiltrated in a high conductivity graphite foam [20]. LiOH-KOH mixture has a melting point of 315 ºC and an enthalpy change of 535 kJ/kg becoming this blend in one of the most interesting PCM media for DSG technology from the point of view of energy density and melting point.

The heat exchange between the LiOH-KOH mixture and steam would be executed in the shell and tube heat exchanger shown in Fig. 2. Thermal transference is maximized by the graphite foam where hydroxides are infiltrated. The steam would flow through the tubes of the equipment while PCM freezes and melts in the shell during the charge-discharge cycles [18]. Although extensive information regarding corrosion performance of metallic alloys in contact with steam has been reported in the state of the art, lack of knowledge has been detected concerning corrosion performance of selected LiOH-KOH mixture at the desired service

temperature [21-27]. Thus, a materials selection analysis should be performed to specify the optimum alloy and associated corrosion allowance for the design of the PCM heat exchanger to be integrated in the TES system of the DSG facilities under discussion. Despite the fact that low corrosion rates are required to reduce the cost of the shell and tubes in this equipment, tubes corrosion allowances minimization is particularly crucial to maximize the exchange between steam and PCM. In conclusion, materials selection performed in this study implies the cost and efficiency optimization of the key equipment involved in the TES system of the DSG plant under evaluation.

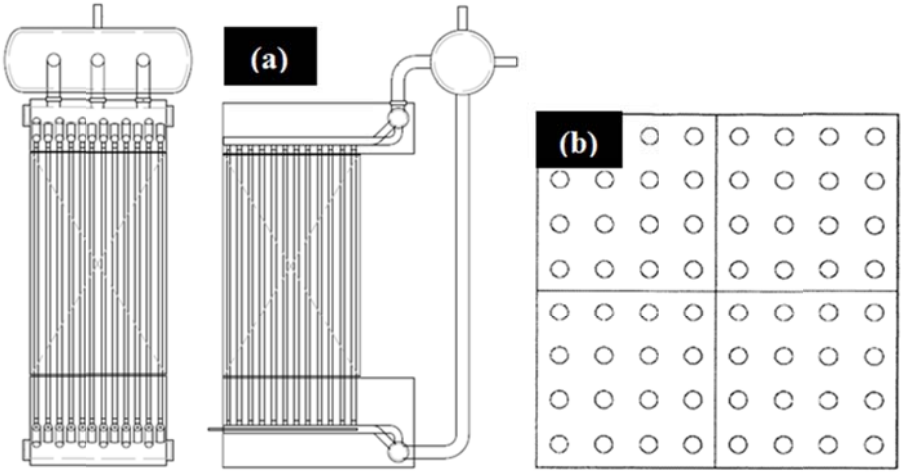

Fig. 2. PCM heat exchanger: (a) PCM heat exchanger sketch, (b) Shell (PCM) & tubes

2. Materials and methods

2.1. PCM

LiOH-KOH mixture was selected as latent storage media due to its high energy density and proper melting point for DSG technology. Selected PCM was a peritectic blend, 46%wt LiOH and 54%wt KOH, as shown in Fig. 3 [28]. Both hydroxides are highly hygroscopic while vapor pressure at high temperature (375 ºC) is low, 1.929 x10^{-8} atm and 1.049 x 10^{-12} atm for KOH and LiOH, respectively [29]. Additional characteristics for these salts, supplied by Sigma Aldrich, are summarized in Table 1 [30].

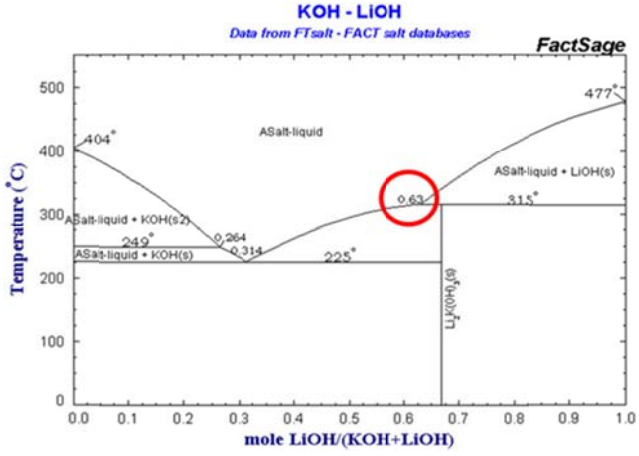

Fig. 3. LiOH-KOH phase diagram [28]

Table 1. LiOH, KOH characteristics [30]

	LiOH	**KOH**
Supplier	Sigma Aldrich	Sigma Aldrich
Reference	442410	60370
Grade	Reagent grade	Puriss. p.a.
Purity	98%	≥ 86%
Form	Pellets	Pellets

2.2. Metal alloys

Three different alloys, A516 Gr70 carbon steel, A316L stainless steel and Inconel 625 Ni-base alloy, were selected to validate the corrosion performance in contact with LiOH-KOH mixture. A516 Gr70 carbon steel is a structural alloy widely used in the manufacture of boilers, storage tanks and pressure vessel in many industrial sectors for low and moderate working temperatures. On the other hand, A316L is an austenitic stainless steel with low carbon content (< 0.03%wt) in order to minimize the tendency of this alloy to form chromium carbides which would precipitate in the grain boundaries producing the material sensitization in the range of 420-850 ºC. Alloying elements in this stainless steel such as Mo (~2%wt) reduce pitting and stress corrosion cracking (SCC) susceptibility. Finally, Inconel 625 is a nickel-chromium alloy used in really highly demanded conditions for its high strength, excellent deformability, weldability and outstanding corrosion resistance. Service temperature for this alloy is fixed in the range from cryogenic to 982 °C. Chemical compositions for materials under evaluation attending to associated standards are exposed in Table 2 and details of these alloys on reception are showed in Fig. 4 [31,32].

Table 2. A516 Gr70, A316L and Inconel 625 chemical composition [31,32]

Alloy	C	Si	Mn	P	S	Cr	Ni	Mo	Fe	Co	Ni	Ti
A516 Gr70	0.31*	0.15-0.30	0.85	0.035	0.035	-	-	-	-	-	-	-
A316L	0.03	1.0	2.0	-	-	16.0-18.0	10.0-14.0	2.0-3.0	-	-	-	-
Inconel 625	0.10	0.50	0.50	-	-	20.0-23.0	58.0**	8.0-10.0	5.0	1.0	3.15-4.15	0.40

* If only one value is given, value shows maximum percentage

** Minimum value for this alloying element

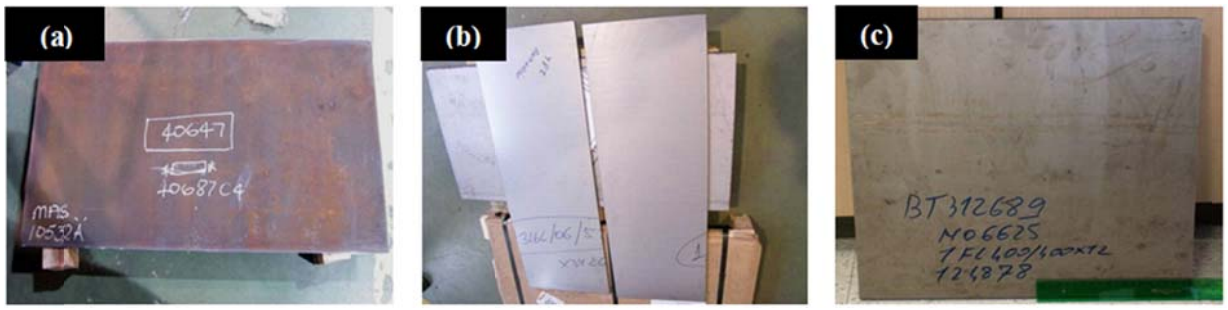

Fig. 4. Materials on reception: (a) A516 Gr70, (b) A316L, (c) Inconel 625

Metal alloys were analyzed by optical microscopy (Motic BA210 trinocular compound microscope) before being exposed to the LiOH-KOH mixture to check associated microstructure and evaluate possible changes after testing (Fig. 5). Accordingly, sections were cut from metal plates and subsequently embedded in resin and polished. A516 Gr70 carbon steel showed a typical ferritic-pearlitic microstructure for this type of steels (Fig. 5a). Meanwhile, A316L stainless steel displayed an austenitic microstructure with ferrite bands (Fig. 5b). Carbides precipitation in the grain boundaries (sensitization) was not observed for this material. Lastly, austenitic microstructure was also detected for Inconel 625 Ni-base alloy (Fig. 5c).

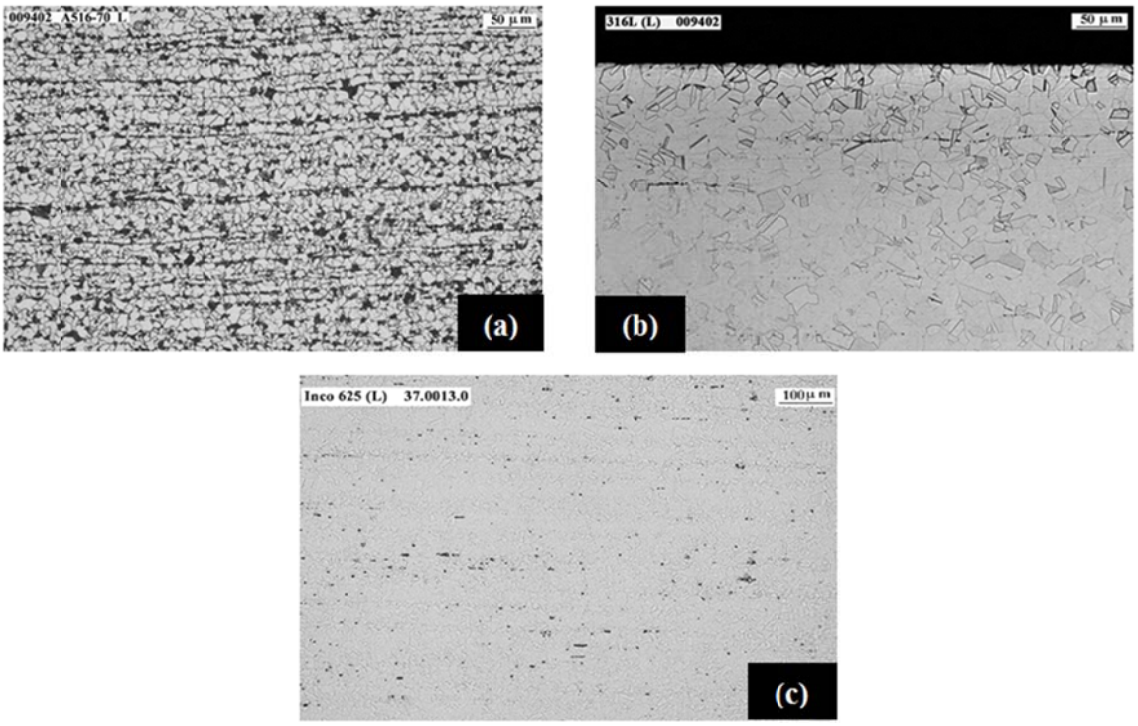

Fig. 5. Materials microstructure before testing: (a) A516 Gr70, (b) A316L, (c) Inconel 625

2.3. Methodology

Thermal treatment was carried out over both hydroxides at temperature in the range of 100-120 ºC in order to remove water content. Then, hydroxides weighting and mixing was performed in a glove box under Argon atmosphere due to high hygroscopicity of these salts. Temperature was fixed at 360 ºC, 45 ºC above mixture melting point, to assure that hydroxides were completely melted. Once carried the salts melting following the peritectic composition, cooling-heating cycles were executed in a ceramic crucible to analyze the performance of the LiOH-KOH mixture. Fig. 6 shows the appearance of hydroxides after heating at 360 ºC during 3.5 hours confirming liquid state at this temperature.

Fig. 6. LiOH-KOH mixture at 360 ºC

The thermal-corrosive treatment was executed in two autoclaves (one for each test time) to simulate operation conditions of the materials under evaluation in contact with hydroxides bath.

Once hydroxides were weighted and mixed in the glove box, the mixture was introduced inside both autoclaves being heated up to 360 ºC under N_2 atmosphere. Temperature was fixed at 360 ºC during several hours to homogenize the mixture. Then, autoclaves were depressurized and opened to introduce corrosion racks with metallic coupons of the three materials under study. Finally, autoclaves were closed being pressurized at 10 bars with N_2 as cover gas. Test temperature was fixed at 360 ºC for both test times, 1005 hours for autoclave 1 and 2640 hours for autoclave 2. Temperature profile was recorded during the test measuring this parameter with three different thermocouples to assure homogeneous temperature inside both reactors.

Different types of metallic coupons were assembled to corrosion racks to evaluate corrosion phenomena such as uniform corrosion, stress corrosion cracking (SCC) and crevice corrosion, among others. Corrosion rack design and metallic coupons detail is shown in Fig. 7. Corrosion rates calculation was performed following guidelines described in ASTM G1-03 taking into account weight loss associated to each material after testing [33]. Accordingly, oxides layers generated during thermal-corrosive treatment were removed by applying a specific chemical etching extracted from this ASTM standard (50% HCl solution plus 3.5 g hexamethylenetetramine for carbon steel, 10% HNO_3 and 2% HF solution for stainless steel and 10% H_2SO_4 solution for Ni-base alloy). Following equation (Eq. 1) was applied to obtain corrosion rates as μm/year:

$$Vc = \frac{\Delta W}{S_0}\frac{K}{t\rho} \qquad \textbf{Eq. 1}$$

where, ΔW is the weight loss of the sample after testing and removing oxide layers (g), S_0 is the initial metallic surface in contact with the corrosive fluid (cm^2), K is a constant to express the final result as μm/year ($8.76x10^7$), t is the exposure time in hours and ρ is the metallic alloy density in g/cm^3. Average corrosion rates were calculated by descaling at least two corrosion coupons of each material. It was assumed that total weight loss was only associated to uniform corrosion without taking into account localized phenomena which were evaluated by other methods. Vc provides an interesting result from engineering point of view to specify corrosion allowances of the heat exchanger where hydroxides will exchange thermal energy with the steam during freezing-melting cycles. Furthermore, corrosion rates obtained from 360 ºC test would include a security factor to specify corrosion allowances for a long term design.

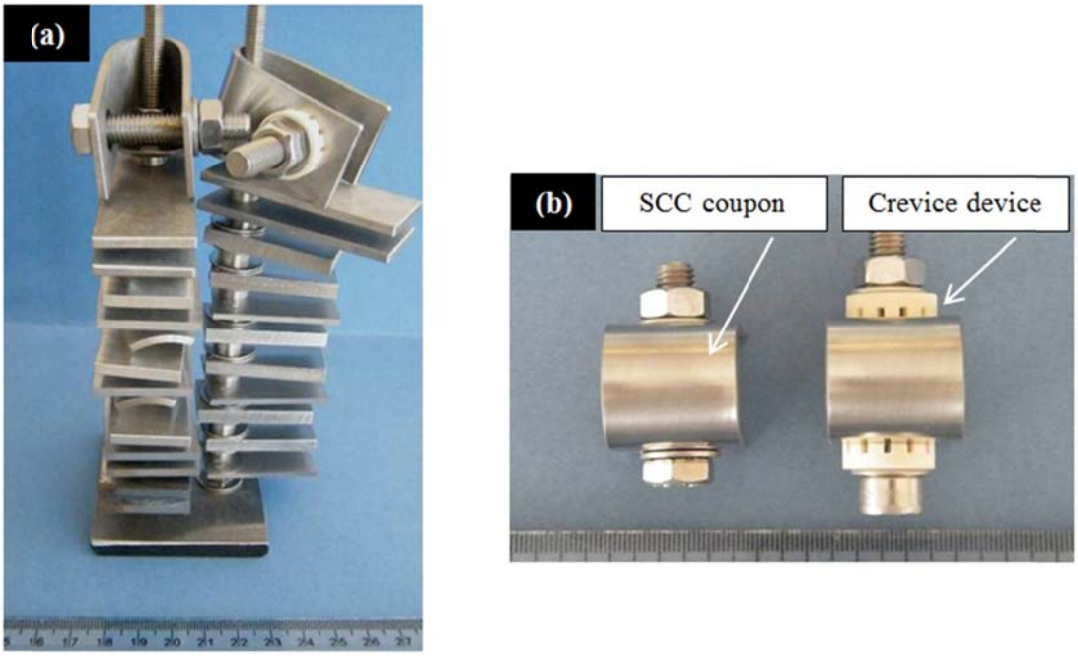

Fig. 7. Corrosion rack: (a) corrosion rack assembly, (b) SCC coupon and alumina device to evaluate crevice susceptibility

SCC phenomena susceptibility was analyzed by evaluating SCC specimens. These types of coupons were welded and bended at 180 ºC maintaining this deformation throughout the corrosion test. Procedure was performed according to ASTM G30-97 and ASTM G58-85 standards characterizing at least two SCC coupons for each material and test time [34,35]. Specimens were analyzed with optical microscopy under low magnification and also by scanning electron microscopy (SEM) to identify possible cracks located in the bending area due to residual stresses coming from welding and bending processes by using SEM-JEOL 5910-LV microscope. On the other hand, ceramic devices were assembled to SCC coupons to identify crevice corrosion sensitivity of tested alloy under hydroxides treatment at 360 ºC. Alumina devices created overlapping surfaces where crevice phenomena could appear as indicated by ASTM G78-01 [36]. In addition to crevice and SCC susceptibility, localized defects such as pitting, intergranular corrosion, selective leaching of alloying elements, among others were also evaluated after testing. Microstructural characterization over corrosion coupons transversal sections was executed by using electron microscopy analyzing phenomena such as oxide morphology and extension of the corrosion damage through material. Energy dispersive spectroscopy (EDS) spectra were performed using a microanalyser (EDS-OXFORD INCAx-act) coupled to SEM to characterize alloying elements evolution thorough oxide layers generated over metallic alloys. Finally, corrosion coupons surfaces were also evaluated by SEM to detect possible spalling phenomena in the oxide layers developed by the material under evaluation.

3. Results and discussion

3.1. Visual inspection

Once corrosion tests were finished, t_1 test time at 1005 hours and t_2 test time at 2640 hours, corrosion racks were extracted from both autoclaves (Fig. 8). Both racks were introduced in ultrasound baths with distilled water at room temperature to remove hydroxides adhered to

metallic specimens. Then, corrosion coupons were dried with alcohol to carry out visual inspection over them.

Fig. 8. Corrosion rack removal

A516 Gr70 carbon steel showed uniform corrosion with a blackish oxide layer generation apparently well adhered and compact for t_1 test time (Fig. 9a). There were no pitting or other localized phenomena detected for this set of coupons. Coupons associated to t_2 test time showed a different appearance. The outermost blackish oxide layers were spalled from the metal showing reddish-brown corrosion products over metal alloy (Fig. 9b). Moreover, A316L stainless steel presented uniform oxides layers for both test times. There were two different types of corrosion products observed, blackish and iridescent oxide layers, over the metal specimens not detecting pitting or other localized phenomena (Fig. 9c-d). Finally, Inconel 625 showed similar performance to A316L stainless steel for both test times generating compact blackish oxide layers not detecting corrosion products spalling, pitting or other defects (Fig. 9 e-f).

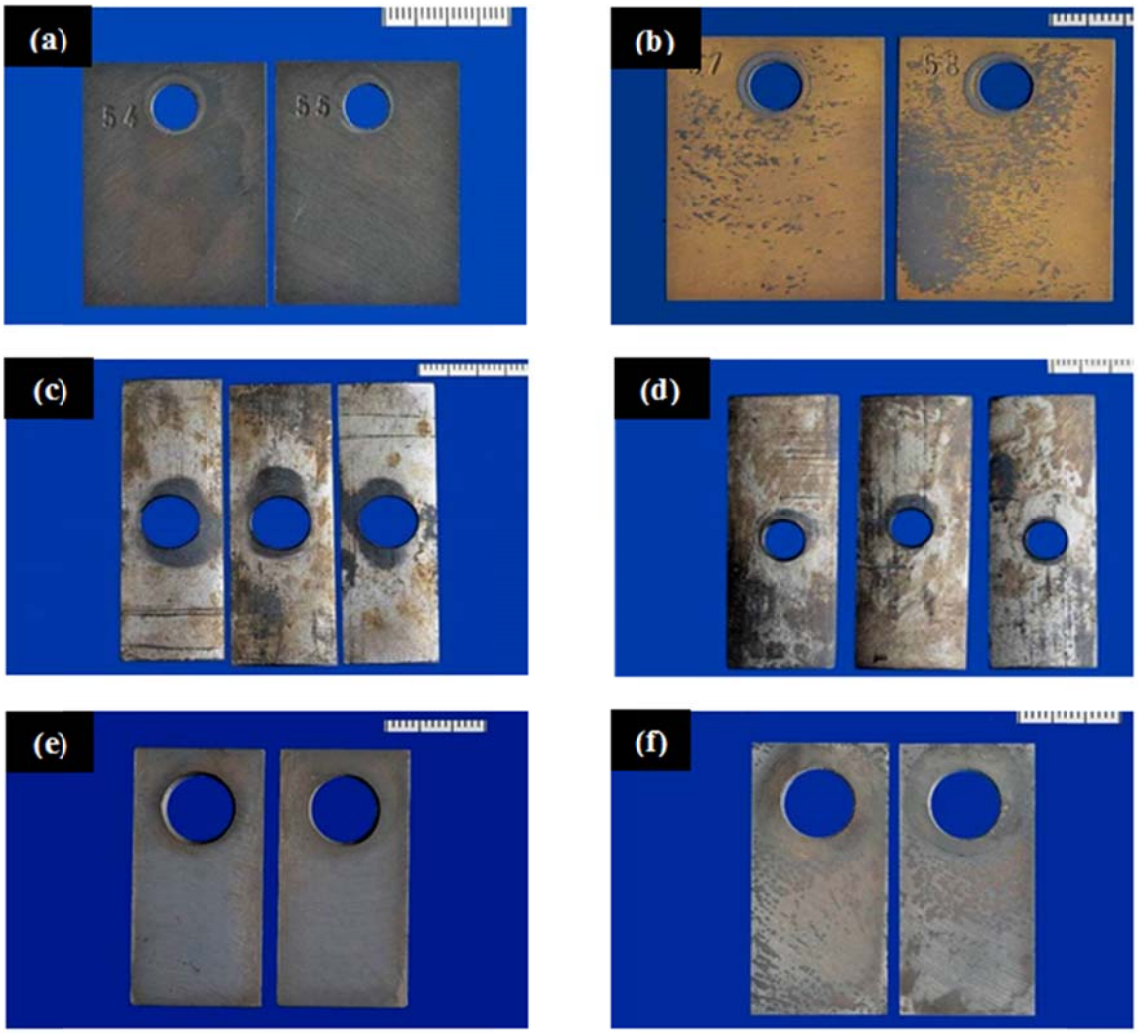

Fig. 9. Corrosion coupons appearance after testing: (a) A516 Gr70 after t_1 test time, (b) A516 Gr70 after t_2 test time, (c) A316L after t_1 test time, (d) A316L after t_2 test time, (e) Inconel 625 after t_1 test time, (f) Inconel 625 after t_2 test time

3.2. Corrosion coupons surface analysis

SEM characterization was performed to evaluate the surface of metal alloys under study. A516 Gr70 micrographs for t_1 and t_2 test times are showed in Fig. 10 (Fig. 10a-b). While oxide layers showed well crystalized and adhered over the base material for t_1, oxides generated during t_2 test time were spalled and broken. Oxide layers performance associated to t_2 test time would imply lack of alloy passivation in addition to generation of non-protective corrosion products. Oxides layers generated over A316L stainless steel coupons were continuous and thinner than those observed for A516 Gr70 (Fig. 10 c-d). Taking into account A316L oxides evolution, steel passivation and corrosion rates reduction would be expected for long term performance. Inconel 625 displayed very similar performance to A316L stainless steel generating adherent, thin and compact oxides layers. Appearance for Inconel 625 after the second test time is shown in Fig. 10 (Fig. 10 e) being coupons conditions very similar after t_1 test time. Accordingly, corrosion rates reduction is also expected for this material.

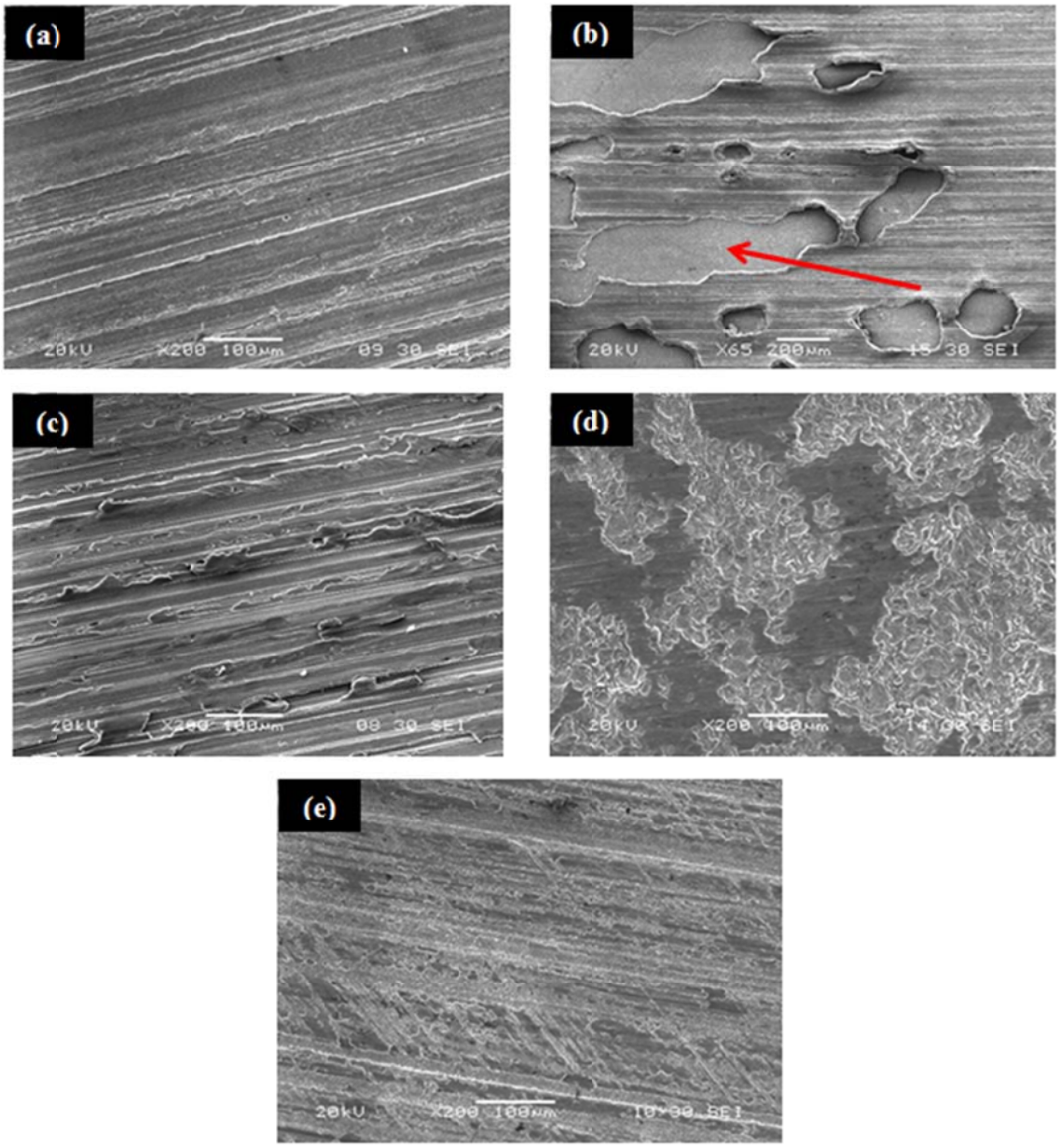

Fig. 10. Coupons surface SEM analysis: (a) A516 Gr70 after t_1 test time, (b) A516 Gr70 after t_2 test time, (c) A316L after t_1 test time, (d) A316L after t_2 test time, (e) Inconel 625 after t_2 test time

3.3. Corrosion coupons transversal section analysis

Metallographic specimens were machined from corrosion coupons of the three materials under evaluation after testing in the hydroxides mixture. Specimens were analyzed by SEM and EDS to analyze oxides morphology and corrosion attack progression through the base material. A516 Gr70 carbon steel showed an oxide layer firmly adhered to the substrate with a uniform thickness in the range of 14-15 µm for t_1 test time (Fig. 11a). Micrograph associated to t_2 test time showed a double oxide layer detected during the analysis of the coupon surface (Fig. 11b). Average thickness for each layer was in the range of 20-24 µm. EDS spectra indicated similar chemical composition for both oxide layers mainly consisted in iron oxide (Fig. 11c). A non-uniform oxide layer was observed for A316L with thickness in the range of 2-7 µm at both test

times. As expected, this layer had a chemical profile mainly composed by Cr, Fe and Ni. Cr-enrichment was detected in the oxide layer closer to the substrate (Fig. 11d). A316L micrographs also showed a slight corrosion penetration through austenitic grain boundaries, intergranular corrosion (IGC), in specific areas (Fig. 11e). This effect increased with the exposure time being the maximum affected depth in the range of 10-12 µm. Inconel 625 Ni-base alloy generated a thin and continuous oxide layer with homogeneous thickness of 7 and 12 µm for 1005 and 2640 hours test time respectively. Compositional profiles for both coupons sets showed a mixed corrosion product with Fe-enrichment in the outermost oxide layer (Fig. 11f-g).

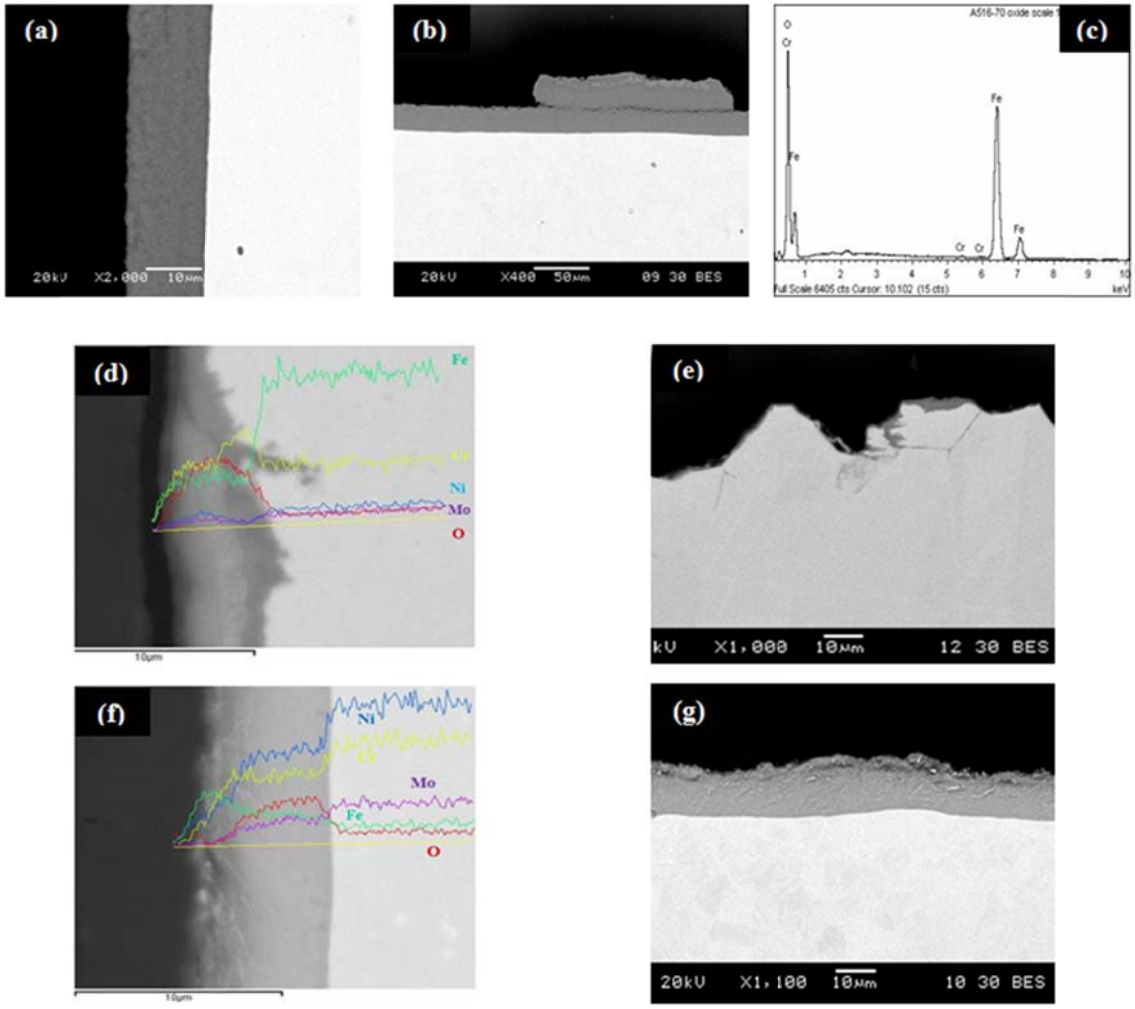

Fig. 11. Transversal sections SEM analysis: (a) A516 Gr70 after t_1 test time, (b) A516 Gr70 after t_2 test time, (c) A516 Gr70 EDS, (d) A316L EDS mapping , (e) A316L IGC detail, (f) Inconel 625 EDS mapping, (g) Inconel after 625 t_2 test time

3.4. SCC and crevice corrosion evaluation

Cracks generation in SCC specimens was not detected after visual inspection for any material under study and both test times (Fig. 12a). Electron micrographs also showed no defects associated to SCC susceptibility. Therefore, Fig. 12 (Fig. 12b) shows a SCC section associated to A316L material where corrosion penetration through grain boundaries was detected without crack development due to SCC sensitivity. Accordingly, the combination material, residual stresses, corrosive media and operation condition simulated within this test was not aggressive enough to produce catastrophic failures in the bending area of these types of alloys. On the other

hand, Fig. 12c shows the deterioration observed in the multi-crevice assembly device after 2640 hours in the LiOH-KOH mixture at 360 ºC. Alumina traces were embedded in the metal surface of the coupons possibly as a result of swelling of the ceramic piece during the thermal-corrosive treatment (Fig. 12d). Ceramic remains were removed by mechanical and chemical treatment to analyze the damage under the multi-crevice device only detecting mechanical defects coming from abrasion processes between ceramic parts and metallic surface (Fig. 12e). In addition, there was not observed crevice attack in other overlapped or occluded areas generated by nuts, spacers, or other elements in the materials under evaluation. In conclusion, A516 Gr70, A316L and Inconel 625 would not be affected by SCC and crevice corrosion phenomena under test conditions.

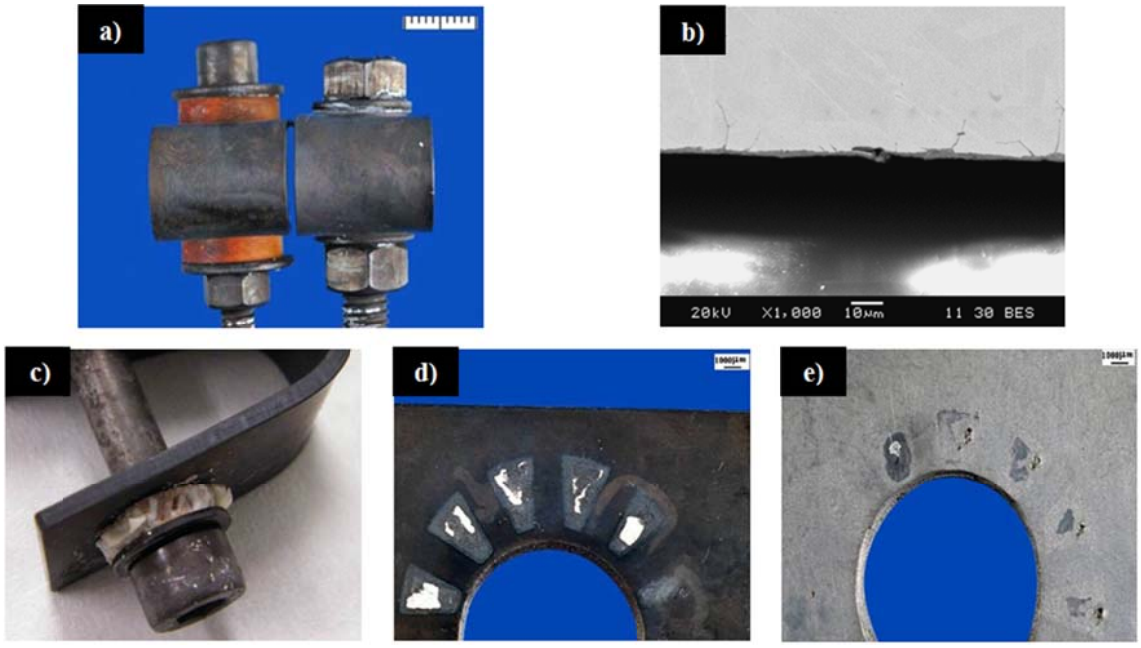

Fig. 12. SCC and crevice specimens: (a) SCC coupons after testing, (b) SCC section micrograph, (c) Multi-crevice device detail, (d) Overlapped area before chemical treatment, (e) Overlapped area after chemical treatment

3.5. Corrosion rates calculation

Corrosion rates values were calculated after testing for both test times to specify corrosion allowances associated to the three materials tested in the hydroxides mixture (Table 3). The guide for corrosion weight loss used in the industry (Table 4) was adapted to A516 Gr70, A316L and Inconel 625 to analyze if these materials were adequate for the construction of steam-PCM heat exchanger to be integrated in the hypothetic CSP plant under consideration [37]. Low corrosion allowances are critical in the design of this equipment to optimize heat transfer between PCM and steam. In addition to corrosion rates as µm/year, weight change after testing (without removing corrosion products) was also included in Table 3 to discuss corrosion phenomena induced by the hydroxides mixture in the carbon steel and stainless steel. A516 Gr70 carbon steel corrosion rates did not present significant decreasing with test time as expected once confirmed spalling processes in the oxide layers. Consequently, corrosion products generated over the base material were not completely protective being this material not recommended for 25 years of continuous operation. Quantitative values associated to A316L

would recommend this material for long term service under operation conditions of this application. Corrosion rates reduction suggested the formation of protective oxide layers. Therefore, parabolic or logarithmic kinetic is expected for long exposure times. Similar performance was detected for Inconel 625 regarding corrosion rates evolution. Although corrosion rates related to Inconel 625 were higher than obtained for A316L, being this material recommended based on the specific application, values decreased with test time demonstrating the passivation of this Ni-base alloy.

Except for the Inconel 625 alloy, the other steels under evaluation experienced negative weight losses after being exposed to hydroxides bath at 360 ºC. Negative weight changes for coupons which display oxide layers over base materials usually indicate that some alloying elements, coming from corrosion products and/or from base material, are removed by the medium being solubilized in the bath. Taking into account that the EDS profiles associated to A516 Gr70 and A316L did not evidenced significant changes in the majority alloying elements in the base material, weight loss should be attributed to certain dissolution of the oxide layers.

Table 3. Corrosion rates for A516 Gr70, A316L and Inconel 625

Test time (hours)	A516 Gr70		A316L		Inconel 625	
	(mg/cm^2)	(µm/year)	(mg/cm^2)	(µm/year)	(mg/cm^2)	(µm/year)
t_1: 1005	-5.8	136	-0.07	10.3	0.30	30.0
t_2: 2640	-21.8	134	0.02	6.3	1.8	15.2

Table 4. Guide for corrosion rates in the industry adapted to A516 Gr70, A316L and Inconel 625 [37]

A516 Gr 70 (µm/year)	A316L (µm/year)	Inconel 625 (µm/year)	Recommendation
> 1275	**> 1253**	**> 1185**	Completely destroyed within days
127 - 1274	**125 - 1252**	**118 - 1184**	Not recommended for service greater than a month
64 - 126	**63 - 124**	**59 - 117**	Not recommended for service greater than 1 year
14 - 63	**13 - 62**	**12 - 58**	Caution recommended, based on the specific application
0.4 - 13	**0.4 - 12**	**0.3 - 11**	Recommended for long term service
< 0.3	**< 0.3**	**< 0.2**	Recommended for long term service; no corrosion, other than as a result of surface cleaning, was evidenced

4. Conclusions

This study evaluates the corrosion performance of three different metal alloys, A516 Gr70 carbon steel, A316L stainless steel and Inconel 625 Ni-base alloy, as container material for the construction of a high temperature PCM heat exchanger for DSG technology. Accordingly, thermal-corrosive treatment were developed within high temperatures autoclaves at different test times.

A516 Gr 70 showed the worst performance after testing in the hydroxide bath at 360 ºC. In addition to high corrosion rates which advice against taking into account this material for a long term design, corrosion products spalling was detected within the second test time. Therefore, iron oxides developed over metal alloys were not as protective as required to achieve full passivation and significant reduction in the corrosion rates after 2640 hours. However, localized corrosion phenomena such as pitting, SCC and crevice susceptibility were not detected for this carbon steel. A316L and Inconel 625 showed low corrosion rates, 6.3 and 15.2 µm/year respectively, being both materials suitable for the application under consideration although caution design should be advised for the Ni-base alloy. Protective and well adhered corrosion products, mainly composed by Fe, Ni and Cr as detected in the EDS mapping, were identified for these alloys expecting parabolic or logarithmic corrosion kinetic profiles for long term performance. Although SCC and crevice corrosion susceptibility was not detected for both materials, slight corrosion progression through grain boundaries was displayed by A316L stainless steel. Nevertheless, IGC attack depth was just limited to 10 µm depth. On the other hand, negative weight changes were measured after testing for A516 Gr70 (t_1 and t_2 test times) and A316L (t_1 test time) in the corrosive medium under evaluation. This effect would be attributed to oxides alloying elements solubilisation in the hydroxides bath. Accordingly, corrosion mechanism would be influenced by dissolution processes of the corrosion products in the LiOH-KOH mixture.

In conclusion, after a technical-economic feasibility study, A316L stainless steel was selected as a first approach for the design of the steam-PCM heat exchanger. In addition to adequate thermal-mechanical properties under operation conditions and good weldability, this material displayed excellent corrosion performance during test time. While A516 Gr70 was ruled out due to high corrosion rates and the development of non-protective oxide layers, Inconel 625 was discarded by cause of higher cost (6 times) and larger corrosion rates (2.4 times) than A316L. Although a materials selection focused on stainless steel such as A316L optimizes the shell and tubes costs and thermal efficiency of the heat exchanger regarding Ni-base alloys, further detailed research would be required to analyze IGC phenomena detected after 2640 hours. Finally, materials selection procedure should analyze carbons steels and stainless steels grades in future studies to optimize the heat exchanger design being Cr-Mo steels and ferritic stainless steels interesting low cost alternatives to A316L stainless steel.

Acknowledgements

The research leading to these results has received funding from CDTI in the project Innterconecta Thesto (ITC-20111050). The work is partially funded by the Spanish government (ENE2011-28269-C03-02, ENE2011-22722, ENE2015-64117-C5-1-R, and ENE2015-64117-C5-2-R). The authors would like to thank the Catalan Government for the quality accreditation given to their research group GREA (2014 SGR 123) and research group DIOPMA (2014 SGR 1543).

References

[1] Cabeza L, Galindo E, Prieto C, Barreneche C, Fernández, A. Key performance indicators in thermal energy storage: Survey and assessment. Renewable Energy, 2015; 83: 820–827

[2] Gil A, Medrano M, Martorell I, Lázaro A, Dolado P, Zalba B, Cabeza L. State of the art on high temperature thermal energy storage for power generation. Part 1 - Concepts, materials and modelization. Renewable and Sustainable Energy Reviews, 2010; 14: 31-55

[3] Herrmann U, Geyer M, Kearney D. Overview on thermal storage systems. Workshop on Thermal Storage for Trough Power Plants. FLABEG Solar International GmbH, 2006

[4] Wagner S, Rubin E. Economic implications of thermal energy storage for concentrated solar thermal power. Renewable Energy, 2014; 61: 81-95

[5] Denholm P, Hummon M. Simulating the Value of Concentrating Solar Power with Thermal Energy Storage in a Production Cost Model. NREL Report No. TP-6A20-56731. Golden, CO: National Renewable Energy Laboratory, 2012.

[6] Hernández-Moro J, Martínez-Duart JM. CSP electricity cost evolution and grid parities based on the IEA roadmaps. Energy Policy, 2012; 41: 184-192

[7] Yogev R, Kribus A. Operation strategies and performance of solar thermal power plants operating from PCM storage. Solar Energy, 2013; 95: 170-180

[8] Xu B, Li P, Chan C. Application of phase change materials for thermal energy storage in concentrated solar thermal power plants: A review to recent developments. Applied Energy, 2015; 160: 286-307

[9] Khan Z, Khan Z, Ghafoor A. A review of performance enhancement of PCM based latent heat storage system within the context of materials, thermal stability and compatibility. Energy conversion and management, 2016; 115: 132-158

[10] Seitz M, Cetin P, Eck M. Thermal Storage Concept for Solar Thermal Power Plants with Direct Steam Generation. Energy Procedia, 2014; 49: 993-1002

[11] Pirasaci T, Goswami Y. Influence of design on performance of a latent heat storage system for a direct steam generation power plant. Applied Energy, 2016; 162: 644-652

[12] Laing D, Bahl C, Bauer T, Lehmann D, Steinmann W. Thermal energy storage for direct steam generation. Solar Energy, 2011; 85: 627-633

[13] Hirsch T, Khenissi A. A systematic comparison on power block efficiencies for CSP plants with direct steam generation. Energy Procedia, 2014; 49: 1165–1176

[14] Feldhoff JF, Benitez D, Eck M, Riffelmann K. Economic Potential of Solar Thermal Power Plants With Direct Steam Generation Compared With HTF Plants. Journal of Solar Energy Engineering, 2010; 132(4): 041001

[15] Birnbaum J, Eck M, Fichtner M, Hirsch T, Lehmann D, Zimmermann G. A Direct Steam Generation Solar Power Plant With Integrated Thermal Storage. Journal of Solar Energy Engineering, 2010; 132(3): 031014

[16] Feldhoff JF, Schmitz K, Eck M, Schnatbaum-Laumann L, Laing D, Ortiz-Vives F, Schulte-Fischedick J. Comparative System Analysis of Parabolic Trough Power Plants with DSG and Oil using Integrated Thermal Energy Storage, Solar Energy, 2012; 86: 520–530

[17] Jové A, Prieto C, Abujas C, Rodríguez-Sánchez A, Alguacil M. Heat storage method and system for a solar steam generation plant and solar steam generation plant. WO 2016/034754

[18] Jové A, Prieto C. Heat storage system and method for the charging and discharging thereof. WO 2014053677 A1

[19] Abe Y, Kamimoto M, Kanari K, Ozawa T, Sakamoto R, Takahashi Y. Peak load coverage by molten salts latent thermal storage. Proceedings of 19th intersociety energy conversion engineering conference; 1984; 2: 1114–1119

[20] Palomo E, Khemis S, Mourand D, Noel F, Ho-Kon-Tiat V, Dauverge JL, Anguy Y, Prieto C, Jové A. Composite material for storing heat energy at high temperatures. EP 2444468 A1

[21] Bozzini B, Barella S, Bogani, F, Giovannelli G, Natali S, Scarselli G, Boniardi M. Corrosion of stainless steel grades in molten NaOH/KOH eutectic at 250 ºC: AISI304 austenitic and 2205 duplex. Materials and Corrosion, 2012; 63: 967-978

[22] Smith G.P, Corrosion of Materials in Fused Hydroxides, OAK Ridge National Laboratory - U.S. Atomic Energy Commission, Report ORNL-2048, 1956

[23] Craighead CM, Smith LA, Jaffee RI. Screening Tests on Metals and Alloys in Contact with Sodium Hydroxide at 1000 and 1500 °F, OAK Ridge National Laboratory - U.S. Atomic Energy Commission, Report BMI-705, 1951

[24] Simmons EM, Miller NE, Stang JH, Weaver C. Corrosion and Components Studies on Systems Containing Fused NaOH, U.S. Atomic Energy Commission, Report BMI-1118, 1956

[25] Lad RA, Simon SL. A Study of Corrosion and Mass Transfer of Nickel by Molten Sodium Hydroxide, Corrosion, 1954; 10 (12): 435-439

[26] Gregory JN, Hodge N, Iredale JVG. The Static Corrosion of Nickel and Other Materials in Molten Caustic Soda, Atomic Energy Research Establishment, Harwell, U.K., 1956

[27] Miller RR. Thermal Properties of Sodium Hydroxide and Lithium Metal, Quarterly Progress Report May, NRL- 3230-201/52, 1952

[28] LiOH-KOH Phase Diagram

http://www.crct.polymtl.ca/fact/phase_diagram.php?file=KOH-LiOH.jpg&dir=FTsalt (accessed 26.04.2016)

[29] Gomez J. High-Temperature Phase Change Materials (PCM) Candidates for Thermal Energy Storage (TES) Applications. National Renewable Energy Laboratory (NREL), 2011

[30] Sigma Aldrich website

www.sigmaaldrich.com (accessed 26.04.2016)

[31] ASM Handbook, Vol.1: Properties and Selection: Iron, Steels and High-Performance Alloys, ASM International, 1990

[32] ASM Speciality Handbook: Nickel, Cobalt and Their alloys, ASM International, 2000

[33] ASTM G1-03. Standard practice for preparing, cleaning and evaluating corrosion test specimens, ASTM International

[34] ASTM G30-95. Standard Practice for Making and Using U-Bend Stress-Corrosion Test Specimens, ASTM International

[35] ASTM G58-85. Standard Practice for Preparation of Stress-Corrosion Test Specimens for Weldments, ASTM International

[36] ASTM G78-01. Standard Guide for Crevice Corrosion Testing of Iron-Base and Nickel-Base Stainless Alloys in Seawater and Other Chloride-Containing Aqueous Environments, ASTM International

[37] V.S. Sastri, E. Ghali, M. Elboujdaini. Corrosion, prevention and protection. Practical solutions, John Wiley & Sons, 2007